PROCEEDINGS A

rspa.royalsocietypublishing.org

Research

Cite this article: Shinde SY, Arakeri JH. 2018 Physics of unsteady thrust and flow generation by a flexible surface flapping in the absence of a free stream. *Proc. R. Soc. A* **474**: 20180519. http://dx.doi.org/10.1098/rspa.2018.0519

Received: 3 August 2018
Accepted: 25 September 2018

Subject Areas:
fluid mechanics, mechanical engineering

Keywords:
flapping foil, flexibility, hovering, fluid–structure interaction, swimming, flying

Author for correspondence:
Sachin Y. Shinde
e-mail: sachin@iitk.ac.in

Physics of unsteady thrust and flow generation by a flexible surface flapping in the absence of a free stream

Sachin Y. Shinde† and Jaywant H. Arakeri

Department of Mechanical Engineering, Indian Institute of Science, Bangalore 560012, India

SYS, 0000-0003-4559-0019

Inspired by the flexible wings and fins of flying and swimming animals, we investigate the flow induced by the interaction between a flapping flexible surface and the surrounding fluid for the limiting case of Strouhal number $St \to \infty$ (zero free-stream speed). The model selected for this purpose is a two-dimensional sinusoidally pitching rigid symmetric foil to which is attached at the trailing edge a thin chordwise flexible surface (along the chord line). The flow so generated is a coherent jet aligned along the foil centreline, containing a reverse Bénard–Kármán vortex street and delivering a corresponding unidirectional thrust. We analyse the flow and thrust generation process. The measured velocity field suggests that the flow and thrust generation mainly occurs during the phases when the trailing edge is near the centreline. Flexibility of the surface is important in accelerating the near-wake flow and in transferring momentum and energy to the fluid. We present a detailed account of when and where the momentum and energy are added to the fluid. This study shows that the deformations of the flexible surface are responsible for generating a favourable pressure gradient along the jet direction, and for the observed unsteady actuator disc-type action.

1. Introduction

Thrust generation is an essential component of all flying and swimming animals and vehicles. The flapping mode of propulsion has been successfully exploited by birds, insects and fish. Force generation by the flapping wings and fins in nature thus has been a major source of

†Present address: Department of Mechanical Engineering, Indian Institute of Technology, Kanpur 208016, India.

Electronic supplementary material is available online at https://dx.doi.org/10.6084/m9.figshare.c.4260713.

THE ROYAL SOCIETY PUBLISHING

inspiration to study oscillating foils for thrust and lift production. Many of the wings and fins are flexible ([1,2] and references therein), and flexibility seems to be an important property that makes possible large changes in the flow, thrust produced and efficiency [3]. The deformed shape plays a key role in determining the flow around these structures, and also in redistributing the forces [1,4–6].

The interactions between fluid and flexible surfaces are inherently complicated and coupled, hence complete analytical models are not yet possible for such intricate interactions. Recently, however, simplified models have been proposed, for example, using linear beam theory [7], small amplitude flapping theory [8,9] and a large amplitude beam model [10]; Tam [11] proposed a reduced order model for a flapping flexible wing and obtained theoretical scalings for the enhancement in lift and wing circulation. Instead of looking for a complete analytical model, some studies approach such interactions differently; for example, Dewey *et al.* [12] proposed scaling laws for thrust development by flapping flexible panels, Gazzola *et al.* [13] proposed scaling for aquatic animals, Lucas *et al.* [14] observed particular bending patterns of the flexible wings and fins of swimming and flying animals during steady cruising and Shelton *et al.* [15] used flapping flexible foils to model the fish propulsion that is achieved by passing undulatory waves along its body. The interactions between fluid and flexible surface are highly complex and many details remain unknown. We approach this intricate problem through experiments and explore the flow physics and the interactions between the fluid and a flapping flexible surface.

While several studies have been carried out for flapping of rigid and flexible foils with forward motion (see reviews [16,17] and references therein), very few deal with the important limit of zero forward speed (e.g. [18–21] for rigid foils and [22–24] for flexible foils), which would have a connection with hovering. In fact, in 2014, Ristroph & Childress [25] developed a jellyfish-like hovering device using four flapping flexible surfaces.

Flexibility in the flapping foils seems to have a prominent influence on both the flow and the thrust generation, and, thus, on the performance. Experiments over flexible foil flapping in uniform flow by David *et al.* [26] showed that the peak thrust and the peak efficiency occur at different values of non-dimensional stiffness of flexible flap. Experiments by Park *et al.* [27] in quiescent water showed that the phase delay between the pitching angle and the bending angle of the trailing edge, which arises as a consequence of flexibility of the pitching panel, has to be $\pi/2$ for maximum thrust production; they further demonstrated that, under such a half-π phase delay condition, the interactions between the vortices generated from the trailing edge are such that they preserve the regions of thrust-generating momentum which contain high streamwise velocities for the longer downstream distances.

Recent studies by Marais *et al.* [28] and Shinde & Arakeri [29] showed that the flexibility in a thrust-generating flapping foil plays a very crucial role in modulating the flow; note that, while the former study is in the presence of free-stream flow, the latter is in the absence of free-stream flow. Shinde & Arakeri [29] have shown that a sinusoidally pitching rigid foil to which a flexible surface is attached at the trailing edge generates a coherent unidirectional jet for the limiting case of reduced frequency and Strouhal number tending to infinity. The jet is composed of a reverse Bénard–Kármán vortex street. A coherent jet is produced, provided the 'effective stiffness' of the flexible surface lies in a particular range of values. Very flexible and very stiff flaps do not produce coherent jets, only 'moderately flexible' ones do. In the present paper, we discuss the details of flow and thrust production from such a flexible foil flapping in the absence of free-stream flow.

A common and useful model for thrust generation is the so-called 'actuator disc model'. An actuator disc is a thin disc which accelerates the fluid passing through it by adding momentum and energy to the fluid. It is common to model a rotating wing as an actuator disc, e.g. the rotor in a hovering helicopter [30]. Various studies also model insect and bird hovering as an actuator disc; however, in these studies the disc is composed of two (one for each flapping wing) areas of circular arcs (usually less than 180°) which are determined by the sweep of the flapping wing [31–33]. Unlike in the case of an aircraft propeller or helicopter rotor, thrust generation in the natural world is unsteady, and a 'pulsed actuator disc model' may be more appropriate [34]. Here we show

that the flexible foil produces accelerating flow in the downstream which is analogous to that produced by an actuator disc, or, more appropriately, an 'unsteady actuator disc'. We show that the observed actuator disc-type action is a consequence of flexibility in the sense that flexibility helps in orienting the pressure gradient in the downstream direction, which is not possible with rigid foils/flaps. Though we report this interesting observation, we do not intend to propose any model for the 'unsteady actuator disc'.

Most earlier studies on flapping foils explore the after-effects of using flexibility, namely performance enhancement in terms of thrust and efficiency characteristics (e.g. [35–37]). The details of unsteady flow and thrust generation, and the intricate interactions between fluid and flexible surface, however, have received little attention. The primary aim of the present paper is to bridge this gap, explore the flow physics and clearly bring forth the crucial role of flexibility in the generation and development of unsteady flow and thrust. We also explain with the help of control volume analysis using momentum and energy calculations when and where the momentum and energy are added to the fluid by the flapping flexible surface. Although our study is for a flexible foil pitching in a quiescent medium, the methodology and the conclusions may be extended to the cases with non-zero free-stream velocities as well.

The contents of the rest of the paper are as follows. Section 2 describes the experiments and §3 the flow. Section 4 deals with the flow and thrust generation mechanisms and demonstrates the role of flexibility; we also present details of flap motion, and discuss how the vortices are generated. This section further discusses how momentum and energy are added to the fluid by the flexible flap, the control volume analysis and the unsteady nature of thrust generation. Towards the end of §4, we briefly present the unsteady actuator disc-type action created by the flexible foil and also discuss the mechanism of pressure gradient generation that is responsible for the actuator disc-type action. Section 5 presents the effect of pitching parameters on the flow and thrust generation. Section 6 contains the main conclusion.

2. Experiments

We conduct experiments in quiescent water in a glass tank ($800 \times 800 \times 350\,\mathrm{mm}^3$). Figure 1*a* shows a schematic of the experimental arrangement. We sinusoidally oscillate the aerofoil in pitching at a fixed location and study the flow in a horizontal plane along the foil mid-span. Below we describe the experimental set-up and diagnostic techniques; however, as they are similar to those used in Shinde & Arakeri [29], we give only the essential details here. Additional information can be found in [38].

We use an aerofoil model, shown in figure 1*b*, which we call a 'flexible foil'. The aerofoil section has a NACA0015 symmetric profile with chord $c = 38$ mm and span 100 mm, and is made from a hard plastic (acrylonitrile butadiene sulfide). To introduce flexibility, we extend the chord beyond the rigid trailing edge by appending a chordwise flexible transparent surface made from 0.05 mm thick polythene sheet (Young's modulus $E = 3.02 \times 10^8\,\mathrm{N\,m^{-2}}$ and flexural stiffness $EI = 3.15 \times 10^{-7}\,\mathrm{N\,m^2}$). The flexible surface deforms only in the chordwise direction. The flexible surface exposed to the fluid is 30 mm along the chord and covers the entire span. Thus, the ratio of flexible to rigid chord is 79%, which is fixed in our experiments. The mass of the flexible surface (0.15 g) is negligible when compared with the added mass of fluid (≈ 70 g, estimated by treating the flexible surface as a two-dimensional plate moving normal to itself). For convenience, we call the 'flexible surface' a 'flexible flap' or just a 'flap' in the rest of the paper.

A servo motor (Panasonic A series) in co-ordination with a Galil motion controller card (DMC–1425) oscillates the aerofoil sinusoidally about a pitching point at 12 mm (0.32*c*) from the leading edge. The pitching motion is prescribed as $\theta = \theta_{\max} \sin(2\pi f t)$, where θ is the instantaneous pitching angle, t is the time, $\theta_{\max}$ is the amplitude and f is the frequency of pitching. The parameters that varied were pitching amplitude ($\theta_{\max} = \pm 10^\circ, \pm 15^\circ, \pm 20^\circ$) and frequency ($f = 1, 2, 3, 4$ Hz for each $\theta_{\max}$). In all, we studied the 12 cases listed in table 1.

We used visualizations and particle image velocimetry (PIV) as the main diagnostics. The field of view was about $190 \times 145\,\mathrm{mm}^2$; however, in some figures, data may be shown in only

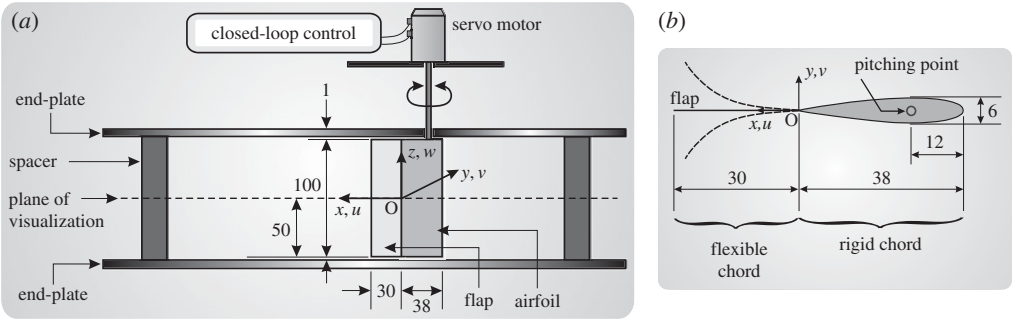

Figure 1. Schematic of the (*a*) experimental set-up and (*b*) aerofoil model—'flexible foil'. All dimensions are in millimetres. Panel (*a*) shows that the aerofoil model is confined between end-plates to ensure two-dimensionality; a gap of about 1 mm between the aerofoil end and the end-plate is provided on either side to allow smooth motion. Spacers between the end-plates are away from the aerofoil so as not to affect the flow. The aerofoil oscillates symmetrically about the zero-angle position of the rigid chord. x, y, z are, respectively, the streamwise, transverse, spanwise directions and u, v, w are the corresponding velocities. We call x the streamwise direction even though there is no free-stream flow.

Table 1. Experimental conditions. Aerofoil performs sinusoidal pitching. Reynolds number is based on $V_{TE_{max}}$ (see text).

amplitude (θ_{max})	frequency (f in Hz)	Reynolds number (Re)
±10°	1	1078
	2	2156
	3	3234
	4	4312
±15°	1	1617
	2	3234
	3	4851
	4	6468
±20°	1	2156
	2	4312
	3	6468
	4	8625

a limited region depending on the requirement. A laser sheet (about 1 mm thick) was used to illuminate the horizontal plane along the aerofoil mid-span. Visualizations were with fluorescein disodium salt (dye) or polystyrene particles, captured using a Kodak Motion Corder Analyzer camera (SR-Ultra, 512 × 480 pixels). The velocity field was obtained with PIV using 30 µm hollow glass spheres (3 M™) as tracers and a Nd:YAG dual pulsed laser (Quantel Big Sky) for illumination. Image pairs were acquired at a rate between 1 and 5 Hz using a SharpVISION™ camera (1360 × 1036 pixels), and processed with the PIV software proVISION–XS™ (IDT) using 32 × 32 pixels interrogation windows with 50% overlap. Spacing between the velocity vectors was 0.064c. The overall error was estimated to be about 1% of the instantaneous maximum streamwise velocity. Our PIV measurements do not resolve the boundary layers around the foil and the flap.

We used two separate optical arrangements, as shown in figure 2. For visualizations, the flap was blackened to trace its motion (figure 2*a*); the aerofoil and flap motions were tracked from the motion of the edge of the shadow. However, for the PIV measurements, the flap was transparent

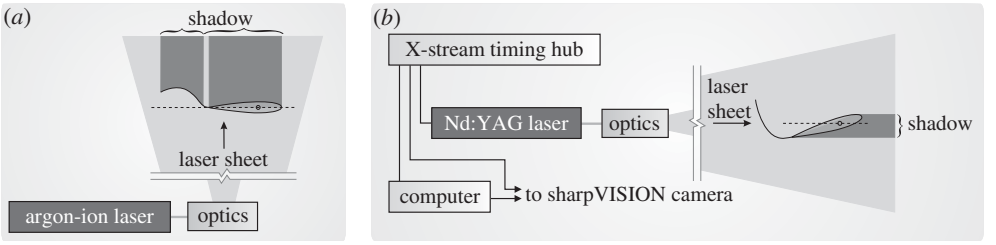

Figure 2. Schematic of the optical arrangement for the (*a*) visualization experiments and (*b*) PIV measurements. For visualizations, the flap was blackened except for a small portion near the TE (about 3 mm) to identify the start of the flap, and the light sheet was passed from the bottom side. For PIV, the flap was transparent to obtain velocity data on both of its sides, and the light sheet was passed from the left side to minimize the shadowed region.

and light passed through (figure 2*b*), which made it possible to obtain velocity data on both of its sides; shadow was only due to the rigid aerofoil. Thus, the velocity data were accurately captured except in a very narrow shadow region where the velocities were anyway small due to zero free-stream speed.

As there was no free-stream flow ($U_\infty = 0$), we defined the Reynolds number based on the maximum velocity of the rigid foil trailing edge ($V_{\mathrm{TE_{max}}}$) as $Re = V_{\mathrm{TE_{max}}} c/\nu$, where ν is the kinematic viscosity of water. The Re range was between 1078 and 8625 for the 12 cases studied (table 1). Our experiments considered one limiting case of the flight regime where the Strouhal number ($St = fA/U_\infty$, where $A = \Delta_{\mathrm{TE_{max}}}$ is the y-amplitude of the rigid foil trailing edge deflection) and reduced frequency ($k = 2\pi fc/U_\infty$) tend to infinity; if defined alternatively using $V_{\mathrm{TE_{max}}}$ and c or $\Delta_{\mathrm{TE_{max}}}$, both St and k turn out to be either a constant or a parameter already listed [29]. Non-dimensional frequencies in the form of the Roshko number ($Ro = fc^2/\nu$) are 1437, 2874, 4310, 5747, respectively, for 1, 2, 3, 4 Hz. In this paper, the abbreviations LE, TE and FT, respectively, denote the leading edge, the trailing edge and the flap tip; for any quantity 'q', we denote the ensemble average by $\langle q \rangle$, time average by $\bar{q}$ and its non-dimensional form by q^*.

3. The flow

The sinusoidal oscillations of the aerofoil with chordwise flexible flap attached at the trailing edge create a coherent, undulating jet aligned along the centreline (figure 3) that has an associated thrust. The jet is composed of vortices arranged in a 'reverse Bénard–Kármán vortex street' configuration. As there is no free stream in the present experiments, it needs to be emphasized that the jet flow is entirely due to the flapping motion of the flexible foil. In the absence of free-stream flow, the jet generated by the flapping foil has the tendency to switch direction [20,22]. Shinde & Arakeri [29] have identified the two underlying mechanisms for suppressing the jet meandering and generating the coherent reverse Bénard–Kármán vortex street and the unidirectional thrust along the centreline: first, appropriate spatial and temporal shedding of the vortices from the flap tip, and, second, convection of the vortices away from the place of shedding. Further, they defined a non-dimensional parameter which includes the effects of fluid–structure interaction, namely 'effective stiffness' $EI^* = 8EI/(1/2\,\rho\, V^2_{\mathrm{TE_{max}}}\, s_\mathrm{f}\, c^3_\mathrm{f})$, which represents the inverse of the flap deflection due to the fluid-dynamic loading; in this expression, EI is the bending stiffness of the flap, ρ is the fluid density, $V_{\mathrm{TE_{max}}}$ is the maximum velocity of the rigid foil trailing edge, s_f is the span and c_f is the chord length of the flexible flap. Based on EI^*, Shinde and Arakeri identified three flow regimes and showed that only for a flap of the appropriate 'effective stiffness' ($0.1 \lesssim EI^* \lesssim 1$) are the coherent and unidirectional jet and thrust produced. We observed that the pitching flexible foil creates the coherent jet for those cases in table 1 which satisfy this criterion.

In this paper, our aim is to understand the mechanism of flow generation and the unsteady nature of thrust generation through control volume analysis, and clearly demonstrate the role of

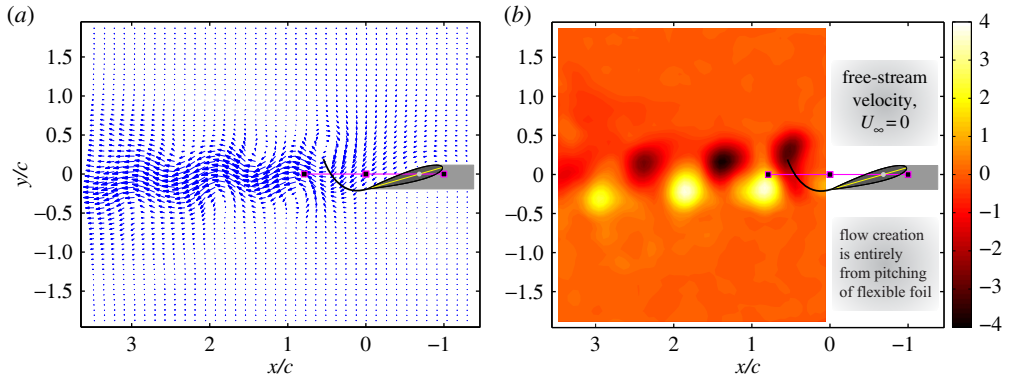

Figure 3. Flow field for the foil with the flexible flap for the standard case ($\theta_{max} = \pm 15^\circ$, $f = 2$ Hz) at one phase when TE is near the extreme location: (*a*) velocity field and (*b*) spanwise vorticity (ω_z) field. A reverse Bénard–Kármán vortex street causing an undulating jet is seen. Vorticity is normalized by $V_{TE_{max}}/\Delta_{TE_{max}}$. Positive is counterclockwise vorticity and vice versa. The laser sheet is passed from the left; the grey patch near the aerofoil shows the shadowed region. The small filled rectangles along $y/c = 0$ from right to left indicate, respectively, the LE, TE, FT locations in the mean position and the grey dot is the pitching point; lines joining the rectangles show the rigid and flexible chords in the mean position. For the sake of clarity, the velocity vectors in (*a*) (and all other subsequent figures showing the velocity field in this paper) are shown at every alternate station in the *x*-direction.

flexibility in these processes. We will also briefly discuss an important observation, namely the 'unsteady actuator disc'-type action which occurs as a consequence of foil flexibility. We are not aware of any study on flapping flexible foils that deals with the details of how the flow and the thrust are generated, especially when there is no externally imposed flow or when the foil is not moving forward.

Most of the discussion up to §5 is for one representative case that falls almost in the middle of the parameter range, namely $\theta_{max} = \pm 15^\circ$ and $f = 2$ Hz ($Re_{TE} = 3234$), which we refer to as the 'standard case'; however, as we will show in §5, many of the general conclusions are valid for other cases as well.

In each cycle, a pair of relatively large counter-rotating vortices along with a chain of smaller vortices (observed in the dye visualization, but not captured by PIV due to insufficient resolution) are shed from the flap tip. The oscillating foil and the flexible flap draw in fluid from the quiescent ambient and accelerate it downstream to create the narrow, undulatory jet as shown in figure 3 (also see electronic supplementary material, Movie S1). The flow generation is intimately linked to the motion of the flexible flap which undergoes very large deformations. We will show in §4 that these large deformations do influence the flow generation. Both aerofoil and flap motions cause fluid motion, and fluid motion in turn influences flap motion. The strong interaction between the flap and the fluid results in the reverse Bénard–Kármán vortex street. The undulating flow in the jet is due to the staggered array of vortices, originally created by the flap, which move under their own induced velocities. Additional details on vortex movement and spatial separation of vortices may be found in Shinde & Arakeri [29].

The time mean flow data in figure 4 show some important features of the flow. The mean streamwise velocity (figure 4*a*) shows a two-dimensional jet-like flow. The flow is symmetric about the centreline and it widens downstream due to entrainment, which is also evident from the *u*-velocity profiles at several downstream locations shown in figure 4*b*. Figure 4*a*,*b* also indicates an interesting feature related to the actuator disc-type action produced by the flexible foil: the flow in the narrow jet continues to accelerate even beyond the flexible flap region and attains the maximum jet velocity further downstream of the flap trailing edge. The mean vorticity field in figure 4*c* shows a different view: two strong counter-rotating vortices, close to the FT location, draw in and accelerate the fluid into the jet; shear layers of the jet portion show up as two long oppositely signed tongues of vorticity.

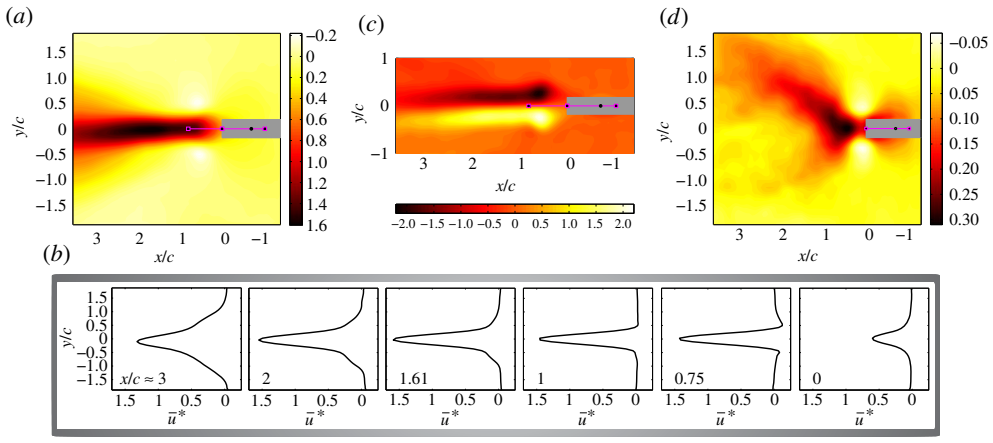

Figure 4. Mean flow data (averaged over 220 flapping cycles). (*a*) Iso-contours of the *u*-velocity for the foil with the flexible flap. The grey patch is the shadowed region due to the rigid foil; data in this region are not shown because they are not available. (*b*) Bottom row: normalized streamwise velocity profiles at several *x*-locations. (*c*) Spanwise vorticity field normalized by $V_{TE_{max}}/\Delta_{TE_{max}}$. (*d*) Iso-contours of the *u*-velocity for the foil without the flexible flap. The flow velocity in (*a*,*b*,*d*) is normalized by $V_{TE_{max}}$. Note in (*a*) and (*b*) that the jet velocity reaches the maximum value downstream of the flap boundary, at $x/c = 1.61$; FT in the undeflected condition is at $x/c = 0.79$.

When the flexible flap is removed, the same foil for the same pitching conditions produces a highly divergent and weak jet as shown in figure 4*d* (see also electronic supplementary material, Movie S2). Shinde & Arakeri [20] have shown that the foil without a flexible flap produces a spread jet that is usually inclined to the centreline and the jet meanders continually and randomly; also, the vortices are not sustained far downstream. Figure 4*a*,*d* shows that the flows from the two foils, with and without the flexible flap, are very different (see electronic supplementary material, movies). However, comparison of the flows from the two aerofoil models is not the subject of the present paper; rather, the primary focus is to determine how the flow is altered as a result of the presence of a flexible surface at the trailing edge.

4. Unsteady flow and thrust generation mechanisms

This section discusses the unsteady mechanism of the flow and thrust generation, and the momentum and energy transfer to the fluid by the flapping flexible foil; emphasis is given to clearly demonstrate the role of flexibility in these processes. We also present the control volume analysis in detail, and briefly discuss the actuator disc-type action produced by the foil as a consequence of foil flexibility.

(a) Flow generation

We observed that the flexible flap alters the flow substantially. To understand how the creation of the jet flow is directly linked to the flap motion and how the unsteady pressure gradients are developed and applied by the flexible foil to create and accelerate the flow, first we need to look at the deformed geometries of the flexible flap.

Figure 5*a* shows the flap profiles over half a cycle for eight phases (named P1–P8). FT trails TE by 137° in the *y*-direction. For most of the cycle (phases P1–P6), some portion of the flap moves in one direction and the remaining portion moves in the opposite direction (e.g. figure 5*b*); only during P6–P8, and the corresponding phases in the other half cycle, does the entire flap move in one direction (e.g. figure 5*c*). When TE and FT move in opposite directions, there will be a point over the flap with zero velocity which we call the 'point of zero velocity' (PoZV). We will

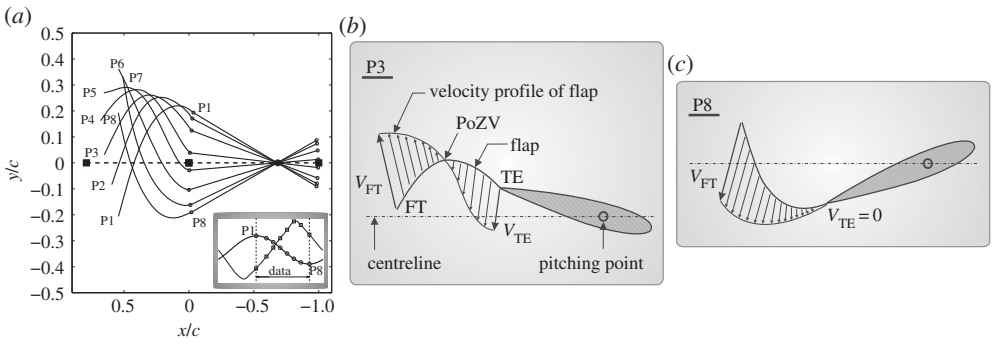

Figure 5. (*a*) The flap profiles at eight phases (P1–P8, $\Delta t \approx 0.07\,\tau$, where τ is the cycle period) over the half cycle when TE moves down; straight lines are the rigid foil chords. Broken lines show the rigid foil chord and the undeflected flap along the centreline. FT deflections are larger in the *y*-direction than the deflections in the *x*-direction. Inset shows the time traces of *y*-deflections of TE (thick line) and FT (thin line) over one cycle; phases P1–P8 are marked (see the electronic supplementary material for all data on FT motion). (*b*) Schematic showing a phase (e.g. P3) when portions of the flap move in the opposite *y*-directions. PoZV is the point of zero *y*-velocity of the flap. (*c*) A phase (e.g. P8) when the entire flap moves in one direction and there is no PoZV.

show later that the PoZV may be related to momentum addition to the fluid and also to vortex formation.

We now describe the physics of flow generation and the main processes that produce the coherent, aligned jet using the flow fields over the half cycle of oscillation shown in figure 6. We also identify the roles of flexibility in the flow generation.

Figure 6 shows the velocity fields for phases P1–P8. At phase P1, TE is at the top-extreme location, the aerofoil is stationary and the entire flap motion is due to the fluid motion created previously. As TE starts to move down, it pulls the flap; thus the rigid foil and the flap portion near TE actively move the fluid. The foil has the maximum velocity at the mean position ($\theta = 0^\circ$). This is when much of the fresh fluid is drawn in and most of the new flow is created, which is clearly seen during phases P4 and P5. During P6–P8, even though the aerofoil and flap decelerate, large fluid velocities are observed near the foil and flap due to the flow created during earlier phases. At P8, foil velocity is zero, and all of the flap motion is passive, similar to P1. The pitching being symmetric, the flow generation during the other half cycle would take place in the same way.

As the reverse Bénard–Kármán jet is composed of vortices shed from the FT, it is important to understand in detail how the vortices are generated. Using the velocity fields in figure 6 and the vorticity fields in the left column of figure 7, we study the generation of a clockwise vortex V3 that is eventually shed just prior to P8. The flow around the flap during phases P2–P6 in figure 6 suggests that the PoZV appears as a moving hinge point about which vortex-like fluid motion is created. Genesis of the clockwise rotating vortex V3 can be seen at P3, and, more clearly, at P4. Almost all the flow associated with this vortex is formed during the active phases P3–P5 (figure 6). The vorticity fields in figure 7 also show the inception of vortex V3 at phase P3. This vortex grows in size as well as strength with time and moves downstream along the flap surface during phases P4–P7. The vortex is finally shed from the flap tip just before P8. For vortex production, the 'pushing and withdrawal' mechanism, similar to that proposed by Taylor [39], seems to be at work. Taylor proposed that 'to generate a vortex ring, give an impulsive motion to a circular disc in quiescent fluid and make it disappear suddenly'; the vortex ring carries the impulse given to the disc. Similar to this mechanism, in the present experiments, the flexible flap pushes the fluid to create vortex-like motion (about the PoZV, which appears as a moving hinge point; see phases P2–P6 in figure 6), and, once created, the flap is withdrawn nearly tangentially (around P7), leaving behind clockwise vortex V3. Movies in the electronic supplementary material clearly depict the flow and the vortex generation mechanisms.

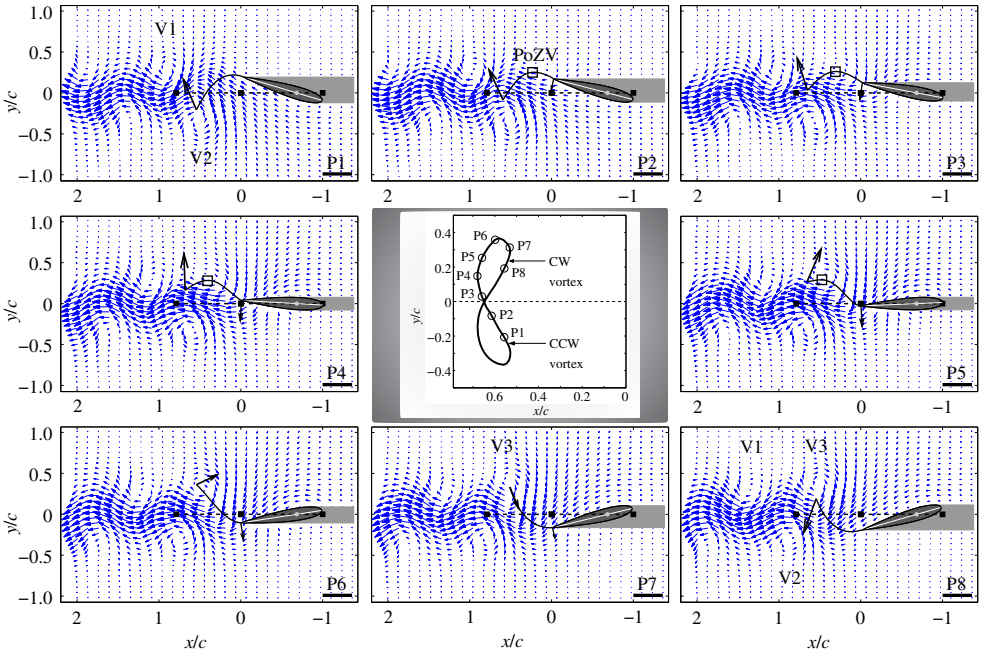

Figure 6. Velocity field at eight phases P1–P8 over a half cycle ($\Delta t \approx 0.07\,\tau$, left to right, top to bottom). Thick arrows at TE and FT indicate their instantaneous velocities; e.g. at P4, $V_{TE} = 83.7$ and $V_{FT} = 148.4$ mm s^{-1}. PoZV (wherever present, shown by a blank square) moves gradually towards FT; it is close to FT at P6. Note, to economize on space, data show a smaller portion of the larger field of view. The panel at the centre of the figure shows the FT locus over one cycle. FT performs a distorted 'figure-of-eight' motion. The dashed line is the undeflected flap along the centreline. The FT positions when a vortex casts off from FT are marked; CW: clockwise and CCW: counterclockwise. Note that, during the active phases P4 and P5 when the TE moves across the centreline, much of the fresh fluid is drawn in by the foil and the flexible flap and thrown downstream into the jet. (Online version in colour.)

The near-wake vortices have a strong influence on the flow, motion of the flexible flap and the subsequent vortex shedding. To understand how, look for instance at the vortices V1 and V2 shed from the flap tip in figure 6 (see phase P1). Note that a part of the flow near the flap and the foil is induced by vortex V2. It can be clearly seen during phases P4 and P5 that, under the influence of vortex V2, the fluid upstream of it turns in the oblique-upward direction, which otherwise is being pushed nearly downward by both the foil and some portion of the flexible flap (from TE up to PoZV). Owing to the combined effect of V2 and the newly created flow, a portion of the flap (between PoZV and FT) is being pushed upward during P2–P5. Because vortex V1 is present above the centreline, the newly created flow moving obliquely upward is turned in the obliquely downward direction. Both V1 and V2 then direct the newly created flow downstream along the centreline.

The deformations of the flexible flap play a significant role in modulating the flow by not just enabling appropriate spatial and temporal release of vortices, but also helping them convect downstream away from the place of shedding. In addition to the velocity induced due to V1 and other wake vortices (figure 6), the downstream motion of the fluid in the flap region (created by the pushing action of the flap and the vortex V2 itself) imparts convective motion to V2 during phases P4–P8. Figures 6 and 7*a* show that V2 is almost stagnant in the x-direction during P1–P4, and its maximum displacement (from $x/c \approx 0.5$–0.75) occurs between P4 and P8. From a travel distance of about a quarter chord in a quarter cycle, its average convective velocity in the downstream direction is estimated to be approximately one chord per cycle.

Another notable feature of the present flow is the absence of leading-edge vortices (LEVs). This is different from previous studies (e.g. [5,18,22–24]), in which both rigid as well as flexible

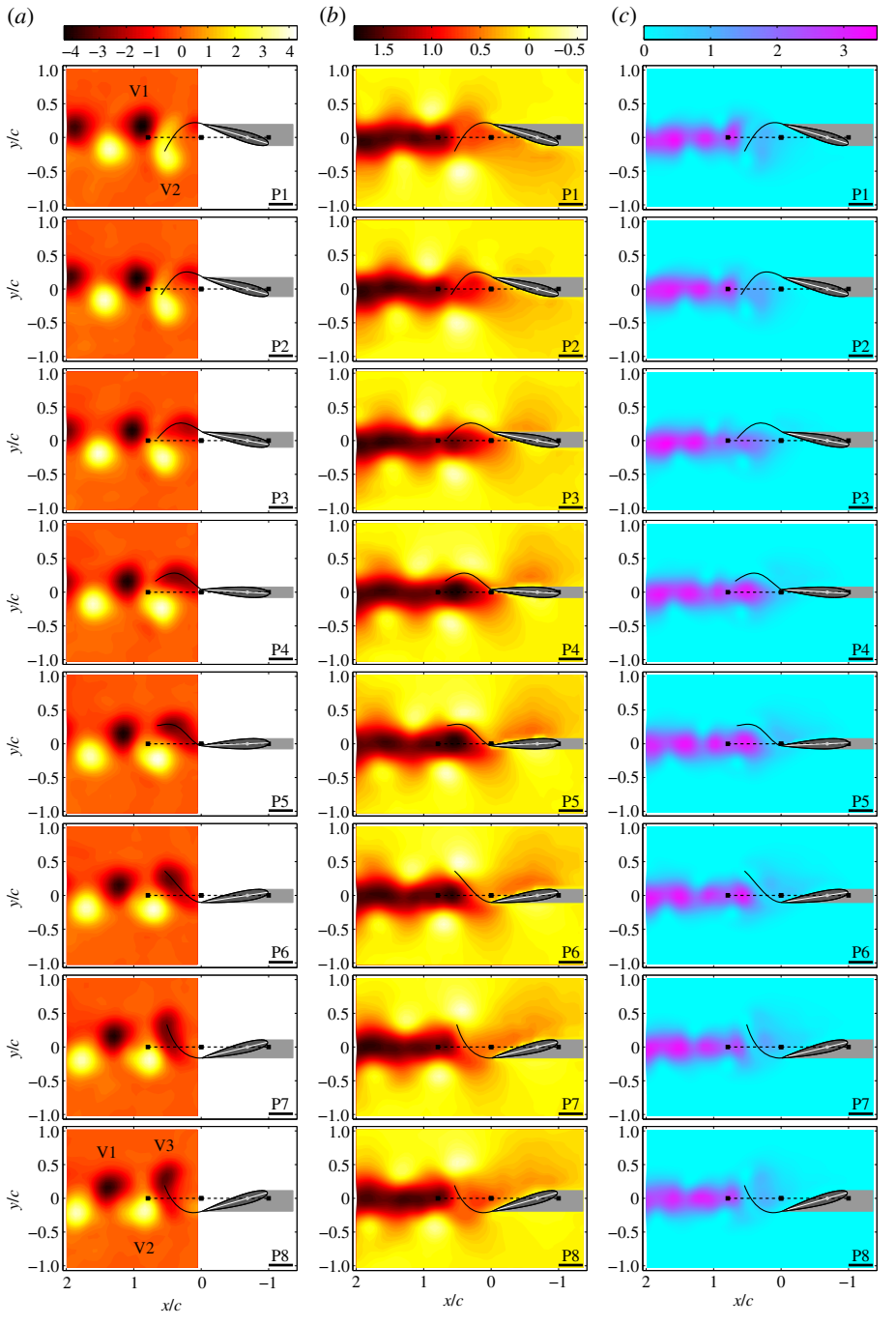

Figure 7. The vorticity (*a*), streamwise velocity (*b*) and kinetic energy (*c*) fields, for phases P1 to P8 for the standard case. Column (*a*) shows the inception, growth and shedding of a CW vortex V3 (see text for details). Columns (*b*) and (*c*), respectively, demonstrate the unsteady process of momentum and energy addition to the fluid by the rigid foil and the flexible flap. Vorticity is normalized by $V_{TE_{max}}/\Delta_{TE_{max}}$, velocity by $V_{TE_{max}}$ and energy by $V^2_{TE_{max}}$.

foil flapping (especially heaving) in still fluid generates LEVs, which form a major component in the flow generated. Dye visualizations clearly showed that the LEVs are not generated in any of the cases studied in the present experiments (e.g. figure 8). These are not produced because the LE is rounded and the pitching point is at only 0.32*c* from the LE, hence there is very little relative motion between the fluid and the rounded LE to cause any vortices there.

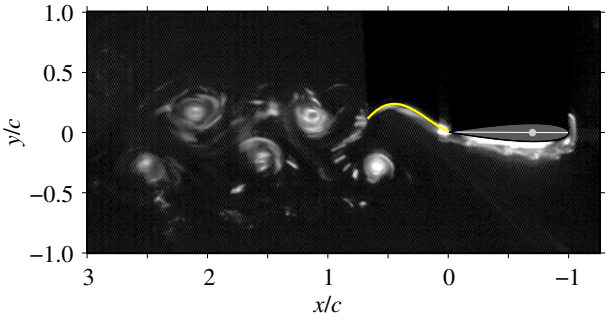

Figure 8. Dye visualization image for the foil with the flexible flap for the standard case at one instant when TE is near the centreline (TE is moving down, FT is moving up). The laser sheet is passed from bottom to top. The small 'blob' of dye near the LE is not a vortex, but it appears because of the following reasons. As there is no free-stream flow, and the foil performs a pitching motion, the following two things happen: (i) dye does not come out of the dye port continuously, but intermittently, and (ii) dye accumulates near the LE because the fluid motion there is small. Therefore, what appears as a vortex near the LE is a 'blob' of dye that is convected by the flow. This feature is clearly seen in the supplementary movie of [29]. (Online version in colour.)

The flow generation process of the narrow jet for the limiting case of the zero free-stream condition can be ascribed to 'the appropriate co-ordination between the motions of the foil and the flexible flap': both foil and flap draw in fluid from the front and largely from the sides, and owing to its deformations the flap pushes the fluid downstream as a jet along the centreline (electronic supplementary material, Movie S1, shows the flow generation process). We are not aware of any experimental study that provides a detailed description of the flow generation process and identifies the role of flexibility.

If the foil with the flexible surface is oriented vertically, then the orderly, narrow jet and the associated thrust generated in an otherwise quiescent ambient is a two-dimensional analogue of the three-dimensional flow structure in the case of natural hovering. The finite span flapping wings of insects and birds generate three-dimensional co-axial vortex rings stacked one upon the other in the vertically downward direction, which produce a jet flowing downward below the animal [33,34,40,41]. The two-dimensional analogue of the stacked vortex rings is a vortex street; such a vortex street is observed downstream of the flapping flexible foil in the present experiments. However, the mechanism of flow and force generation, which comes from the appropriate co-ordination between the motions of the foil and the flexible flap, is different from the 'standard' mechanisms present in birds and insects, where the lift force is essentially from circulation around the translating wing [42,43].

(b) Unsteady momentum and energy transfer

The jet in the present experiments is different from the jet issuing out of a nozzle. The difference is in the way it is created: all the momentum and energy in the jet reported here is generated entirely by the oscillatory pitching motion of the foil.

Some insight into the processes by which momentum and energy are added to the fluid can be obtained from the streamwise momentum (which essentially is the streamwise velocity) and the kinetic energy fields shown, respectively, in columns (*b*) and (*c*) of figure 7 in conjunction with the flow pictures in figure 6 corresponding to phases P1–P8. These columns in figure 7 pictorially show the regions where streamwise momentum and fluid kinetic energy are added, and how these regions move with time. The time series images indicate that the ambient stationary fluid is drawn in during P1 to about P4–P5 and given momentum and energy by the motions of both the flexible flap and the rigid aerofoil. Momentum and energy in the flap region are small during P1 and P2, and they start to increase around P3. The fluid in the flap region shows large momentum

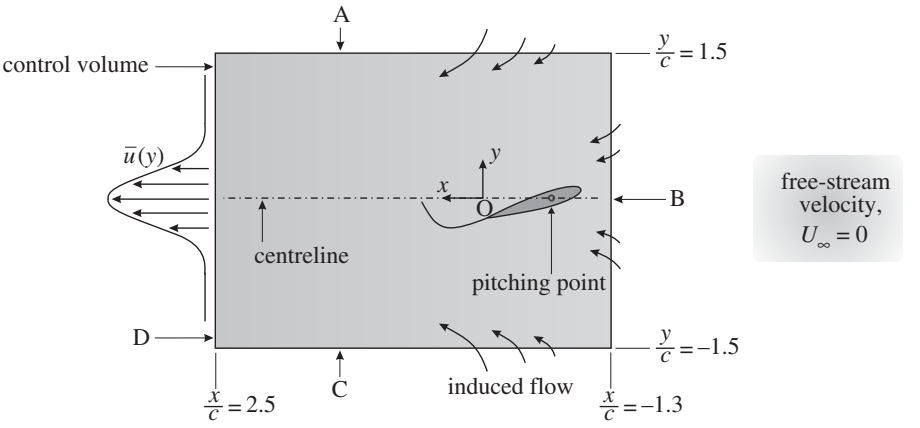

Figure 9. Schematic of the control volume (CV) used for the terms shown in figure 10. Inflow to the control volume is only due to the fluid motion induced by the motions of the foil and the flexible flap.

and energy during phases P4 and P5; this is the time when the rigid foil TE moves with high velocity (with maximum velocity when TE crosses the centreline) and when much of the fresh fluid is drawn in. We may call this the 'active period' when large momentum and energy are added to the fluid. During P6–P8, the foil slows down and consequently the momentum and energy of the fluid in the flap region reduce; however, during this time the bent flexible flap seems to push further downstream the newly created flow of high momentum and energy fluid present just downstream of the flap region. It appears from figure 7 that vortices help to move the high momentum and energy fluid in the downstream direction along the centreline. Remarkably, figure 7 shows that almost all of the momentum and energy addition occurs in the flexible flap region, whereas very small addition takes place in the rigid foil region. Figure 7 also indicates that the vorticity, momentum and energy are highly concentrated around the centreline just within $y/c \approx \pm 0.5$ with very small, almost negligible, values of these quantities beyond $y/c \approx \pm 0.5$; these observations thus strongly emphasize the narrow and coherent nature of the jet along the centreline.

It is evident that the flow and the momentum and energy addition are unsteady, the details of which can be obtained from integral analysis using a fixed control volume (CV) shown in figure 9. At any instant, the streamwise momentum balance and the energy equation for this two-dimensional control volume are, respectively,

$$\langle F_x \rangle = \underbrace{\frac{\mathrm{d}}{\mathrm{d}t}\left\{\int_x \int_y \rho \langle u \rangle \, \mathrm{d}y \, \mathrm{d}x\right\}}_{M_{\text{unsteady}}} + \underbrace{\int_l \rho \langle u \rangle \langle \mathbf{V} \cdot \hat{\mathbf{n}} \rangle \, \mathrm{d}l}_{M_{\text{flux}}}, \tag{4.1}$$

$$-\langle \dot{W}_s \rangle - \langle \dot{W}_p \rangle = \underbrace{\frac{\mathrm{d}}{\mathrm{d}t}\left\{\int_x \int_y \frac{1}{2}\rho\left[\langle u \rangle^2 + \langle v \rangle^2\right] \mathrm{d}y \, \mathrm{d}x\right\}}_{E_{\text{unsteady}}} + \underbrace{\int_l \frac{1}{2}\rho\left[\langle u \rangle^2 + \langle v \rangle^2\right] \langle \mathbf{V} \cdot \hat{\mathbf{n}} \rangle \, \mathrm{d}l}_{E_{\text{flux}}}, \tag{4.2}$$

where $\langle F_x \rangle$ is the force acting on the foil in the x-direction, $\langle \dot{W}_s \rangle$ and $\langle \dot{W}_p \rangle$ are, respectively, the rates of mechanical and pressure work (done at the four faces of control volume), ρ is the density of water and $\mathrm{d}l$ is the elemental distance along the control surface of length l. The first term on the right-hand side of equations (4.1) and (4.2) (unsteady terms) indicates, respectively, the temporal variation of the momentum content (M_{unsteady}) and the energy content (E_{unsteady}) within the control volume; the second term on the right-hand side (flux terms) indicates the momentum flux (M_{flux}) and the energy flux (E_{flux}) across its four faces. Note that $\langle F_x \rangle$ in equation (4.1), apart

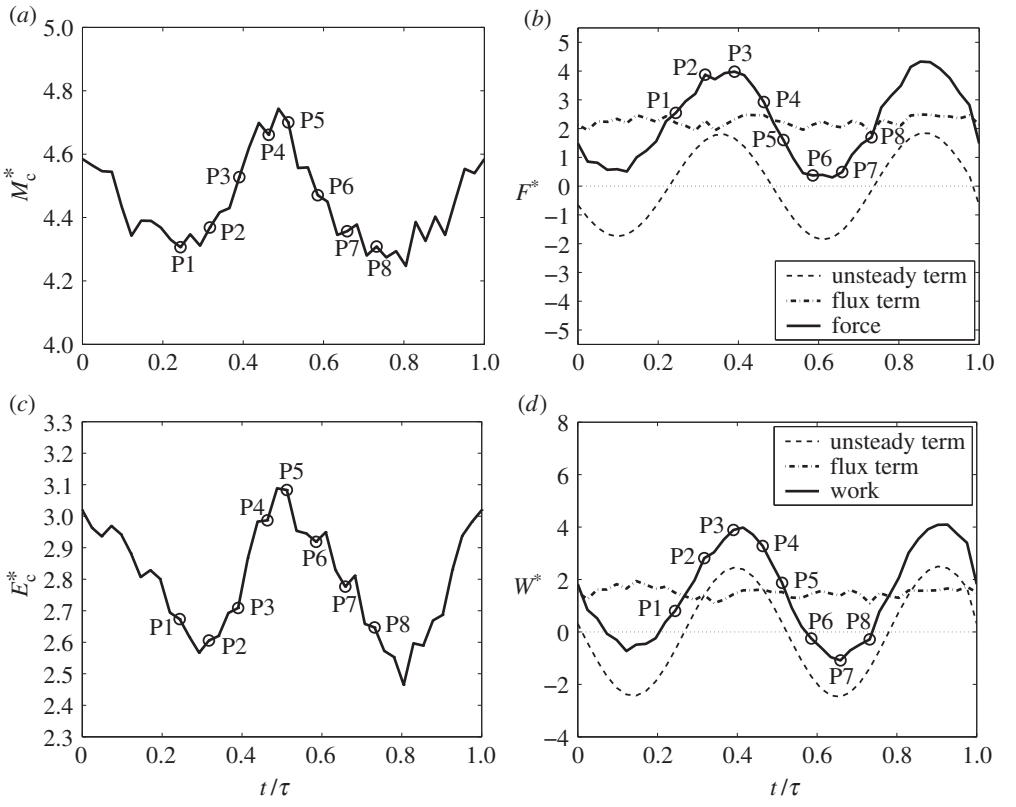

Figure 10. The variation over one pitching cycle of the streamwise momentum (*a*,*b*) and energy (*c*,*d*) for the control volume shown in figure 9. (*a*) Momentum content within the control volume. (*b*) Force and the terms in equation (4.1) non-dimensionalized by $(0.5\rho V_{TE_{max}}^2 c)$. (*c*) Energy content within the control volume. (*d*) Work and the terms in equation (4.2) non-dimensionalized by $(0.5\rho V_{TE_{max}}^3 c)$. $M_c^* = \{\int_x \int_y \rho \langle u \rangle \, dy dx\}/\{0.5\rho V_{TE_{max}} c^2\}$; $E_c^* = \{\int_x \int_y (1/2)\rho[\langle u \rangle^2 + \langle v \rangle^2] dy \, dx\}/\{0.5\rho V_{TE_{max}}^2 c^2\}$. Unsteady terms in (*b*) and (*d*) are obtained by differentiating the curve fitted to the data in (*a*) and (*c*), respectively.

from the force on the foil, may have contributions coming from the unsteady fluid pressure on the control surface [44].

The contributions to the instantaneous force come from the two terms in equation (4.1): (i) the rate at which the streamwise momentum within the CV changes, and (ii) the instantaneous flux of momentum passing through the four faces of the control volume. The instantaneous rate of work also has these two similar contributions in equation (4.2). As we have seen in figure 7*b*,*c*, the high momentum and energy fluid near the flap region travels downstream and eventually moves out of the control surface (D), which shows up as the flux terms in equations (4.1) and (4.2). At the outset, we pointed out that, for both momentum and energy, the flux contribution is almost entirely from the downstream face (D). The momentum and energy flux contributions from the other three faces (A, B, C) are significantly small as the velocities at these three faces are very small; the maximum value of the non-dimensional flux among all these three faces is 0.0612 for momentum and 0.0068 for energy, which are, respectively, about two orders and three orders of magnitude smaller than the corresponding maximum values at face D (see the electronic supplementary material for the variation with time of momentum and energy fluxes over the CV faces).

Figure 10*a* shows the variation of streamwise momentum content within the control volume over one cycle. The eight phases P1–P8 shown in figures 6 and 7 are also marked on this figure in order to connect the observations with the flow. The TE moves between two extreme positions

at P1 and P8, with maximum TE velocity between P4 and P5 when it crosses the centreline. The momentum content (figure 10*a*) is minimum when the trailing edge of the rigid foil is in the extreme positions and its velocity is zero; it increases with time and reaches a maximum between P4 and P5 when the TE velocity is also maximum and when much of the fresh fluid is drawn in (figure 6). The momentum content within the control volume decreases during P6–P8 when the foil slows down. Kinetic energy content also shows a similar variation with time as seen from figure 10*c*. These trends are consistent with the above-mentioned observations.

Figure 10*b* shows that the momentum flux term M_{flux} in equation (4.1) is nearly constant with time and the time derivative of the momentum content M_{unsteady} in equation (4.1) is time periodic with a zero mean; both these terms contribute to the force. The total force (the sum of these two contributions) varies between nearly zero (at around P6) to a normalized maximum value of about 4 at around P2–P3. From the energy balance shown in figure 10*d*, we see that the maximum work is done around P3, again with the flux term being nearly constant and the unsteady part coming from the energy content term that shows time periodic variation with a zero mean. The unsteady analysis for transverse momentum is given in the electronic supplementary material.

Figure 7 shows that much of the momentum and energy addition to the fluid takes place in the flexible flap region compared with the rigid foil region. A large part of the momentum and energy addition is expected to happen at the flap surface. It may be useful to divide the flexible flap into two portions based on its action: *active* (defined as that surface which moves the fluid and adds momentum and energy to it) and *passive* (which is pushed by the existing fluid motion). The flap-end that is firmly attached to the TE is bound to move with it, thus following the prescribed sinusoidal motion. The motion of the rest of the flap is determined by this prescribed motion, and, in addition, by its interaction with the fluid. At any part of the cycle, the active portion of the flap will be doing work on the fluid and adding momentum to it. We can roughly say that, on the active portion, the pressure difference across the flap and motion of the flap are in opposite directions. In the passive portion of the flap, it is likely that some energy is removed from the fluid and the flap extracts work from the fluid; for instance, as seen in figure 10*d*, during phases P6–P8 the work is negative, indicating that the fluid is doing work on the foil and the flap. It is clear that, when $\theta = \theta_{\max}$, the trailing edge is stationary and the entire flap motion is passive. We can see that the flap portion near the TE will largely be active, whereas that near the FT will largely be passive. The proportions of the active and passive portions change with time. We believe that the PoZV may be useful in demarcating the 'active–passive' division of the flap (figure 5*b*). However, precise identification of the active and passive portions demands detailed investigation which is beyond the scope of the present measurements; this will be considered in future. We surmise that such an 'active–passive' division of any flexible surface would provide useful insight towards understanding the action of flexibility in the momentum and energy transfer to the fluid.

The role of the active portion of the flexible flap has been demonstrated in terms of flow generation and momentum—energy addition to the fluid. It appears that the passive portion of the flap is important in appropriate positioning of the vortices, and thus in maintaining proper spacing among the vortices in the reverse Bénard–Kármán vortex street (figures 6 and 7*a*). It is clear that, if the length of the flap is reduced, the vortices casting off from the FT would be placed close to each other. Further study with different length flaps can elucidate the exact role of the passive portion of the flexible flap.

(c) Flapping flexible foil as an unsteady actuator *slab*

We will explain here the interesting flow feature seen in figures 4*a*,*b*, namely the actuator disc-type flow. An actuator disc is a thin disc which accelerates the fluid passing through it by adding momentum and energy to the fluid. A pressure jump (Δp) produces a favourable pressure gradient and accelerating flow both upstream and downstream of the disc (figure 11). The actuator disc is a good model for propulsive devices, including during hovering motion [45].

Figure 12 shows that the structure of the mean flow from the pitching foil with the flexible flap in the present experiments resembles the flow from an idealized actuator disc. The streamlines

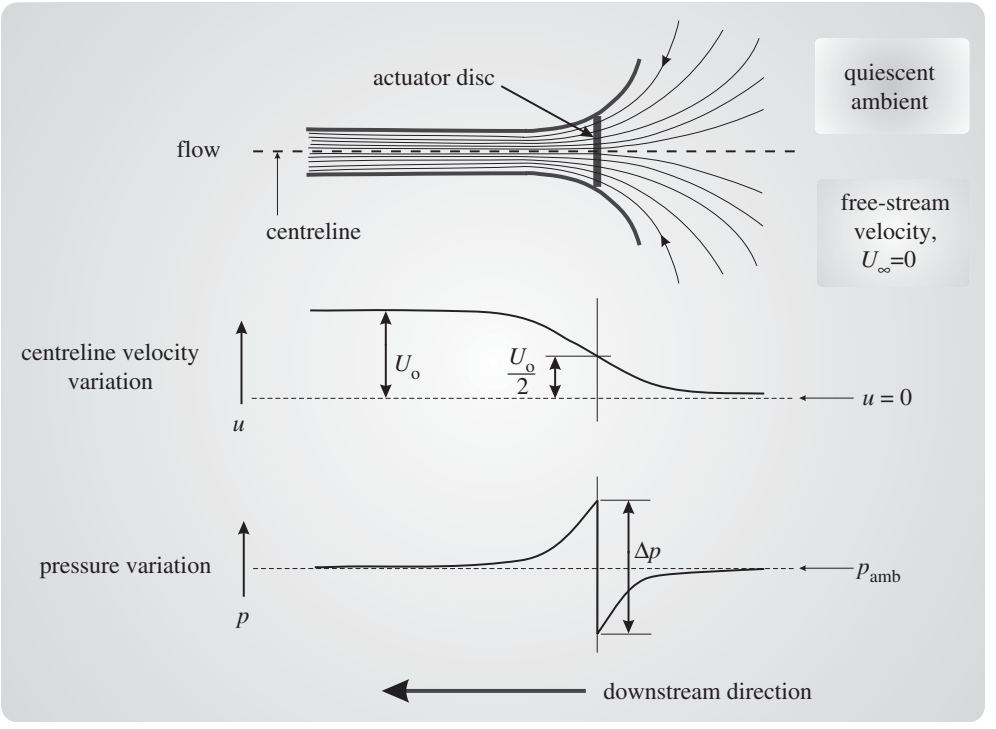

Figure 11. Schematic of the ideal actuator disc for zero free-stream condition. It schematically shows streamlines, and variation of velocity and pressure along the centreline; variation of axial momentum flux will be the same as axial velocity. Here U_0 is centreline velocity far downstream, Δp is pressure jump at the actuator disc and p_{amb} is ambient pressure.

(figure 12*a*), the centreline velocity (figure 12*b*) and the streamwise momentum flux (figure 12*c*) show similar features to the ideal actuator disc model (figure 11). The centreline velocity increases rapidly up to $x/c \approx 0.6$ (figure 12*b*); it continues to increase (but at a slower rate) and reaches the maximum at $x/c = 1.61$, beyond which it reduces gradually. The momentum flux ($\bar{M}_x = \rho \int_y \overline{u^2}\, \mathrm{d}y$) increases slowly in the rigid foil region (figure 12*c*), and rapidly between $x/c \approx 0$ and 0.6, where the motion of the flexible flap adds momentum to the fluid; thereafter, it increases gradually up to $x/c \approx 2.5$, beyond which it remains nearly constant. As in the actuator disc model, the increase in the centreline velocity and the momentum flux downstream of the flap is due to a favourable pressure gradient, which is created there by the action of the flexible flap. These observations raise the question of 'how is this pressure gradient created?' The process by which this pressure gradient is set up is discussed in §4d.

While the flow field from the pitching flexible foil shows many similarities to the idealized actuator disc case, there are important differences, as outlined below.

(i) An actuator disc is a very thin disc rotating about its centre. The pitching flexible foil in the present experiments is fairly long, over which pressure increases. Therefore, the more appropriate name for it would perhaps be an 'actuator slab'.
(ii) In the idealized actuator disc case, velocity in the far downstream and mass flux remain constant. In contrast, for a viscous fluid, due to entrainment, the mass flux increases continuously and the centreline velocity decreases beyond $x/c \approx 1.61$; in this region, the flow is similar to that in a two-dimensional submerged jet.
(iii) The momentum flux increase in the downstream region is similar to the momentum increase in the idealized actuator disc case. But, unlike in the idealized case where no

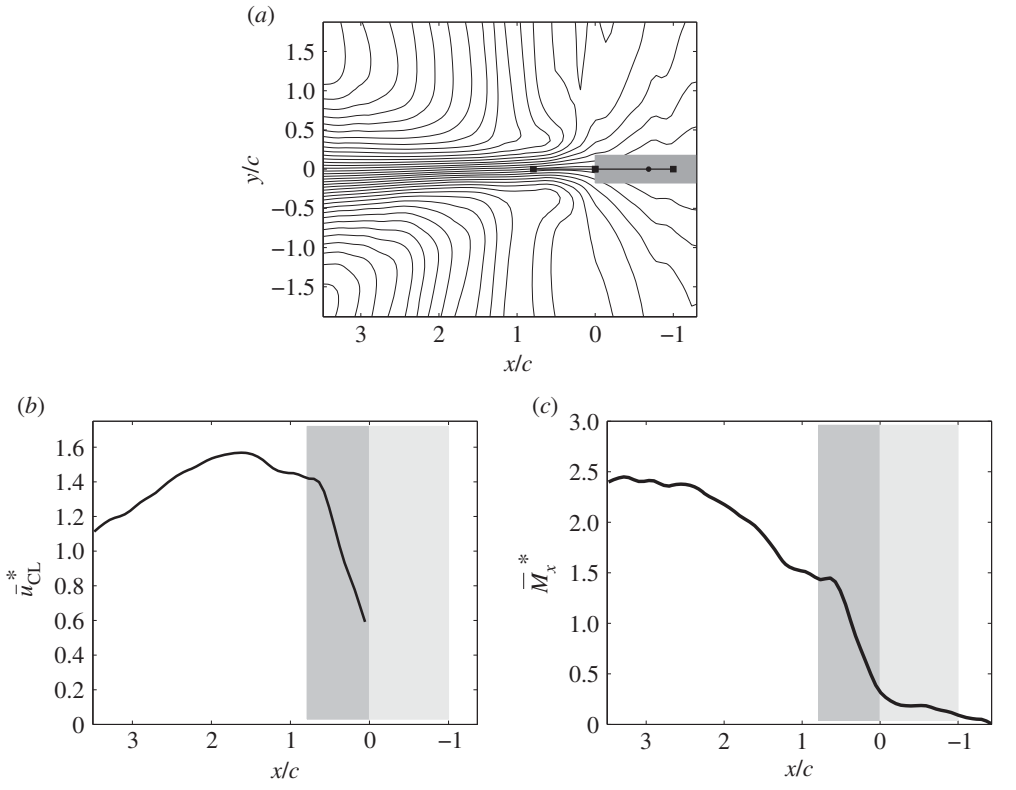

Figure 12. Mean flow data for the flapping foil with the flexible flap for the standard case ($\theta_{max} = \pm 15^\circ$, $f = 2$ Hz) showing resemblance of the flow structure to that from the idealized actuator disc shown schematically in figure 11. (*a*) Streamlines obtained from stream function $\bar{\psi} = \int \bar{u}\, dy - \int \bar{v}\, dx$, normalized by ($V_{TE_{max}} c$). (*b*) Variation with the streamwise direction of the centreline velocity normalized by $V_{TE_{max}}$. (*c*) Variation with the *x*-direction of the mean streamwise momentum flux non-dimensionalized by ($0.5\rho V^2_{TE_{max}} c$). In (*b*,*c*), the highlighted areas show the regions of rigid foil (light shading) and flexible flap (dark shading). The actuator disc type of action comes from the flexible flap region.

momentum increase takes place across the disc, there is a large momentum increase in the flap region in our case.

(iv) The important difference is that the flow is steady in the idealized case whereas in the present case it is unsteady; in fact, it is periodic in time due to the sinusoidal pitching of the flexible foil. We have seen that most of the momentum and energy are added only during some phases, namely the 'active period', which is when most of the contribution to the actuator disc-type action arises. Therefore, the flapping flexible foil may more suitably be thought of as an 'unsteady actuator slab', where the pressure difference and velocity in the slipstream are functions of time.

For hovering of insects, Ellington [34] proposed a 'pulsed actuator disc' model wherein the beating wings apply non-uniform pressure impulses to air. However, an analogous actuator disc modelling of a flapping foil is not known to us so far. It needs to be emphasized that we do not attempt to propose a model for the unsteady actuator disc; instead, we explain the observation of flow acceleration and actuator disc-type action, which comes as a consequence of the presence of flexibility in the foil (as will be shown in §4d).

Note that the differences (ii) and (iii) would be present for any real propulsive device such as a helicopter rotor.

(d) Generation of a favourable pressure gradient

How is the pressure difference in the streamwise direction, which essentially brings in the unsteady actuator disc-type action, created by the flexible surface? As seen in §4b, a pressure difference would exist across any actively moving surface, rigid as well as flexible. Nevertheless, in order to advantageously utilize the fluid dynamic pressure force, its appropriate orientation is very important. Previous studies have shown that flexibility redistributes the fluid dynamic pressure and enhances the thrust and performance for the flapping foils as well as in swimming and flying animals (see [1,4,46] and references therein).

The pressure difference across the flexible flap in the present experiments is created by its motion. For the moving flap, a higher pressure would exist on the front side of the active portion of the flap and a lower pressure on its rear side (figure 13*a*). As there is no imposed flow in our case, pressure differences across the foil and flap are the only sources for the generation of the flow. The deformations of the flexible flap ensure that the active portion remains inclined with the centreline, especially when the TE crosses the centreline ($\theta = 0^\circ$); for example, see phases P4 and P5 in figure 6. Thus, during the active phases, the pressure gradient across the flexible flap is oriented largely in the streamwise direction (figure 13*a*,*b*), causing the (unsteady) actuator disc-type action. The pressure variation locally in the vicinity of the active portion of the flap (as shown schematically in figure 13*a*) will be similar to the one in the idealized actuator disc (figure 11), except that it will be inclined to the centreline unlike in the ideal actuator disc case, where it is exactly along the centreline direction. Ideally, therefore, the active portion of the flap should be as close to the vertical as possible, such that the pressure gradient is in the downstream direction. Deformation of the flexible flap largely achieves this condition, especially during the active phases when much of the new flow is created. Thus, the flap deformations are the ones which bring in the observed actuator disc-type action. One can easily see that, in the case of a completely rigid flap, a similar pressure difference would exist across the entire flap length; however, as the flap does not deform and its angle to the vertical is close to 90°, the pressure gradient will largely be in the transverse direction, as shown schematically in figure 13*c*. Figure 13*d* shows the pressure gradient across the rigid foil without the flap, and figure 13*e* shows the corresponding flow field. The pressure gradient in the case of the rigid foil also would be nearly in the transverse direction. Estimation of the pressure field surrounding the flexible flap would prove the conjecture made in this section.

5. Effect of pitching parameters on flow and thrust generation

We studied the flow for 12 cases by varying the amplitude and frequency of pitching (table 1). Shinde & Arakeri [29] have shown that the flap deformations increase significantly with increasing flapping amplitude and frequency. This is evident, for example, from the cases corresponding to $\pm 15^\circ$ amplitude of flapping, as shown in figure 14: flap becomes increasingly distorted as frequency increases.

Figure 14, which shows the velocity and vorticity fields (for $\theta_{max} = \pm 15^\circ$), indicates that, despite several differences in flap motion, a jet containing a reverse Bénard–Kármán vortex street is generated by the same mechanism as described in §4a; this is true for all the other cases in table 1. However, further downstream, a narrow jet aligned along the centreline is observed only when the effective stiffness is in a particular range ($0.1 \lesssim EI^* \lesssim 1$) [29]. The near-wake flows are almost similar, perhaps because the motions of the active flap portions (which importantly are always near the TE) are nearly similar, and it is only in the passive portions where the large differences in flap geometry occur (see, for example, the near-wake flows and the flap deformations in figure 14) [38]. These changes in the passive portion affect the vortex shedding locations. Moreover, the large changes in the motion of the flexible flap do not have much influence on the overall pattern of vortex shedding (which can be observed clearly from figure 14*d*–*i*): as in the standard case (§4a), the vortices are shed when the FT moves towards the centreline from either side of the centreline, and away from the TE. The main difference is that

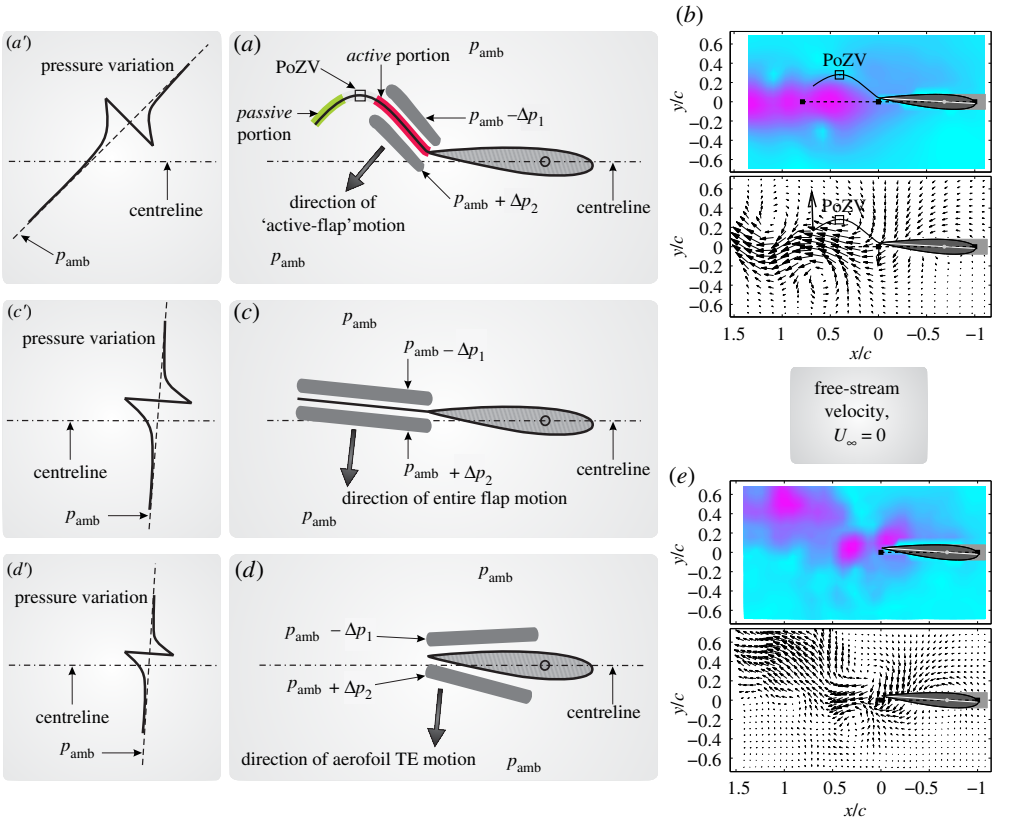

Figure 13. Schematic showing the possible mechanism of generation of a favourable pressure gradient in the streamwise direction; also shown are the flow fields at one instant from the present experiments. Three cases are shown when the TE is moving down: (*a*,*b*) foil with flexible flap, (*c*) foil with rigid flap, (*d*,*e*) foil without a flap. Schematics of the pressure variation are also shown. Here p_{amb} is the ambient pressure and Δp_1 and Δp_2 are the pressure differences. The grey patches drawn ahead of and behind the flexible flap in (*a*), rigid flap in (*c*) and rigid foil in (*d*) show, respectively, the regions of high pressure (i.e. above the ambient pressure) and low pressure (i.e. below the ambient pressure); note that these regions are shown exaggerated for the sake of clarity. (*a*) Schematic of the pressure gradient across the active portion of the flexible flap that creates the flow shown in (*b*); in the active portion of the flap, higher pressure will be obtained on the 'pushing' side of the flap. (*b*) The flow (the contours show the velocity magnitude and the vectors show the velocity field) for the foil with the flexible flap at phase P4. (*c*) Schematic of how the pressure gradient will act if the same flap as shown in (*a*) is made completely rigid. (*d*) The pressure difference associated with the flow shown in (*e*) for the rigid foil without the flexible flap. In (*e*), the contours show the velocity magnitude and the vectors show the velocity field. Schematics in the left column (*a*′,*c*′,*d*′) show the variation of pressure and its inclination with the centreline corresponding to the respective cases in (*a*,*c*,*d*); dashed line indicates ambient pressure. The deformation of the flexible flap orients the pressure gradient in the downstream direction and causes the actuator disc-type action. On the contrary, in the cases of completely rigid flap as well as only the rigid foil (*c*′,*d*′), the pressure gradient is largely oriented in the transverse direction. (Online version in colour.)

the flap deformation increases and the x-location of vortex shedding shifts closer towards the TE location with the increase in the flapping frequency (figure 14*d*–*i*). Again, these features related to vortex shedding have been observed to be similar for the other cases corresponding to $\pm 10^\circ$ and $\pm 20^\circ$ amplitudes of flapping.

The mean flow data show that in all 12 cases the flow accelerates even beyond the flap region and attains maximum velocity somewhere further downstream (figure 15*a*), similar to the standard case discussed in §4. Thus, the actuator disc-type action is present in all 12 cases spanning a sufficiently wide range of flapping amplitudes and frequencies. Figure 15*a* shows that the distance of the streamwise location (x/c) of the maximum jet velocity decreases (i.e. it shifts

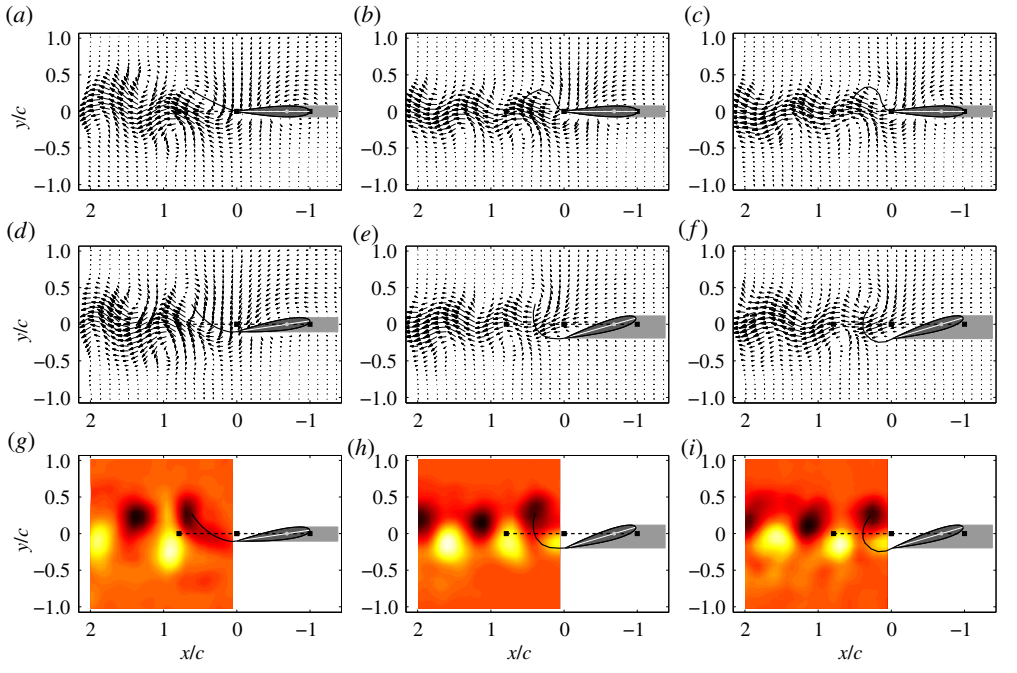

Figure 14. Velocity fields for the cases with $\theta_{max} = \pm 15^{\circ}$: (*a*,*d*,*g*) $f = 1$ Hz, (*b*,*e*,*h*) $f = 3$ Hz, (*c*,*f*,*i*) $f = 4$ Hz. (*a–c*) show the flow field at one phase when the TE is at the centreline and is moving down. (*d–f*) show the velocity and (*g–i*) show the vorticity fields at the time when a clockwise vortex is being shed; the case for $f = 2$ Hz is shown in figures 6 and 7. In general, at the time of shedding of the clockwise vortex, the TE is near the extreme location and almost the entire flap moves passively. With the increase in flapping frequency, the flap becomes more distorted, and also the vortex shedding location moves towards the TE location.

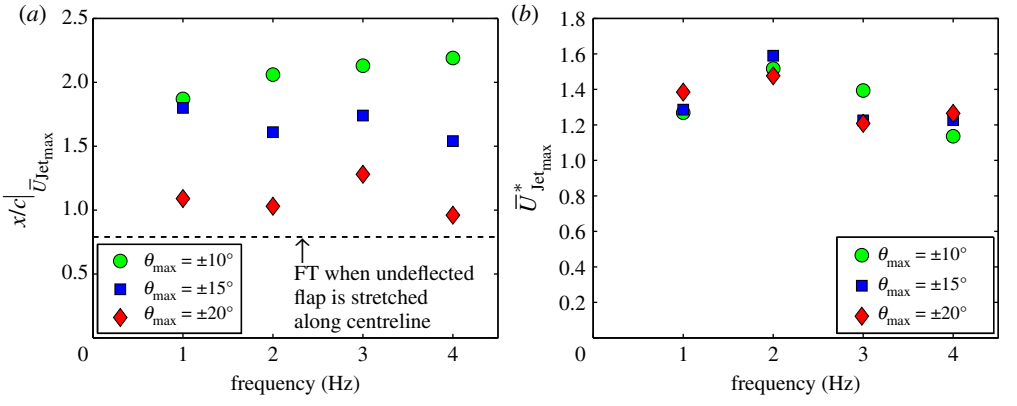

Figure 15. Time mean flow data for the 12 cases in table 1. (*a*) The streamwise location of occurrence of the mean maximum jet velocity. In all cases, the maximum velocity occurs downstream of the flap region, i.e. above the broken line, thus indicating the presence of actuator disc-type action. (*b*) Mean maximum jet velocity normalized by $V_{TE_{max}}$. (Online version in colour.)

towards the TE location, $x/c = 0$) with amplitude, but it is reasonably constant with frequency for a given amplitude. Interestingly, the maximum jet velocity when non-dimensionalized by the maximum velocity of the trailing edge shows that it does not vary much with amplitude for a given frequency (figure 15*b*), thus suggesting that the maximum jet velocity scales with $V_{TE_{max}}$.

One main difference, with change in amplitude and frequency of flapping, is in the nature of momentum addition. In all cases, the increase in mean streamwise momentum flux takes place in

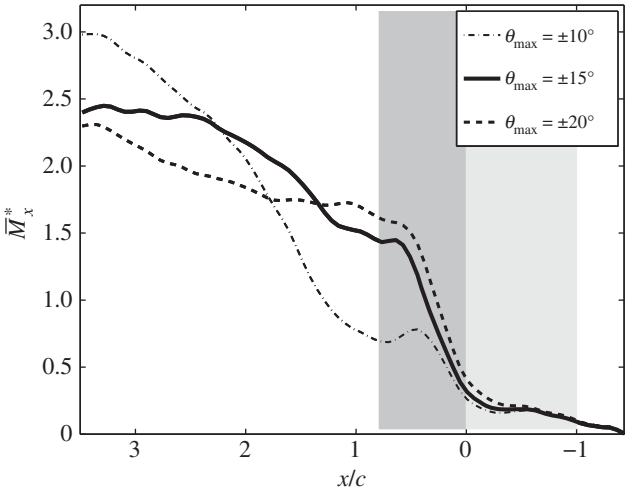

Figure 16. Variation with the x-direction of the time mean streamwise momentum flux non-dimensionalized by $(0.5\rho V^2_{TE_{max}} c)$ for one representative case of 2 Hz frequency for each flapping amplitude in table 1.

two regions: (i) flap region ($x/c \approx 0$–0.8), and (ii) downstream of it ($x/c \approx 0.8$–2.5). For the standard case, the increase is roughly divided equally (figure 12*c*): a rapid rise in the flap region followed by a gradual rise in the downstream region. Some general observations about the momentum addition, as shown in figure 16 for some representative cases, can be made for the other cases [38]: (i) $\theta_{max} = \pm 10°$: a large portion of the increase (about 75–80% of the total) is downstream of the flap; (ii) $\theta_{max} = \pm 15°$: the increases are nearly equal in the two regions; (iii) $\theta_{max} = \pm 20°$: most of the increase (about 65–70%) is in the flap region. This trend—that more of the momentum increase occurs in the downstream region for $\theta_{max} = \pm 10°$ and the increase is mostly in the flap region for $\theta_{max} = \pm 20°$—is consistent with the above-mentioned observation that the location where maximum jet velocity occurs moves towards the TE location with the increase in flapping amplitude.

We calculate the mean thrust coefficient ($\bar{C}_T$) using the integral momentum balance for the mean velocity field; the details of the calculation and the values of the mean thrust coefficients are presented by Shinde & Arakeri [29]. The thrust coefficient is based on the maximum TE velocity ($V_{TE_{max}}$) and the chord (c). Our thrust coefficients ($\bar{C}_T \sim 1.34$–2.13) are similar to those reported previously for the rigid and flexible wings flapping in still fluid (e.g. [18,19,22–24]), however, there are two important distinctions: (i) in these earlier studies the LEVs form a major component of the flow and contribute significantly to thrust generation, whereas in our case the thrust generation is without the LEVs; (ii) they use combined heaving–pitching motion while we use simple rotary oscillations, i.e. pitching.

6. Conclusion

We studied the flow produced by a flexible surface flapping in the absence of free-stream flow ($St \to \infty$). The symmetric foil with a flexible surface attached at its trailing edge generates a coherent, narrow jet (and the corresponding thrust) along the centreline while pitching at a fixed location. The jet is confined within just half a chord distance on either side of the centreline. Without the flexible surface, the foil generates a weak, widespread, meandering jet. A flexible surface is crucial in generating the narrow, orderly jet that is useful for thrust production. While Shinde & Arakeri [29] identified the fundamental mechanisms underlying the generation of such a jet, we explored here the physics of the unsteady flow and thrust generation by the flexible foil, and the intricately coupled interaction between the fluid and the flexible surface. With zero free

stream, the flapping motion of the foil is entirely responsible for the creation of the jet composed of vortices arranged in the reverse Bénard–Kármán street pattern. Flow generation is intimately linked to the motion of the flexible surface, which undergoes large deformations. Measured flow fields showed that it is the appropriate coordination between the motions of the fluid and the flexible surface which create the narrow jet. Vortices are generated possibly by a 'pushing and withdrawal' mechanism similar to that proposed by Taylor [39]. Near-wake vortices show a strong influence on flow generation. The flow and thrust generation mechanism is robust over a wide range of pitching parameters. Thrust coefficients from integral momentum analysis are similar to those in previous studies, which report that LEVs contribute significantly to thrust while LEVs are absent in our case.

This limiting case of $St \to \infty$ is relevant to the hovering flight regime. If the flexible foil is oriented vertically, the unidirectional jet and thrust created in an otherwise quiescent ambient is a two-dimensional analogue of the three-dimensional flow structure in the case of natural hovering. However, the mechanism of flow and thrust generation is different from the 'standard' mechanisms present in nature.

Control volume (CV) analysis is performed to identify when and where the momentum and energy are added to the fluid. Large momentum and energy addition occurs only during some specific part of the cycle, which may be termed the 'active period'—it is that part of the cycle when the TE velocity is near maximum (i.e. when the TE moves around the centreline). The flexible surface is usefully divided into two portions: active (located near the TE) and passive (located near the free end of the flexible surface). Based on the flow data, it may be conjectured that, at any instant, it is the active portion that does work on the fluid and adds momentum to it, whereas the passive portion (being moved by existing fluid motion) determines the location of the vortex shedding. This kind of 'active–passive' division would be a useful way to think of the action of flexible surfaces in general, and needs further investigation. During the active period, the rigid foil and active portion of the flexible surface draw in fluid largely from the sides, impart momentum and energy to it and throw it downstream as a narrow jet. A significantly large fraction of the momentum and energy flux is observed at the downstream face of the CV (about 2–3 orders of magnitude higher than those at the other faces). Contributions to force and work on the CV come from the flux and unsteady terms; while the flux term contributes nearly steadily, the unsteady term shows time periodic variation with zero mean. Interestingly, almost all of the momentum and energy addition takes place across the flexible surface while there is very little addition by the rigid foil.

The mean flow resembles the flow associated with an idealized actuator disc; however, with some important differences: first, pressure gradients are generated over a finite distance as opposed to the localized pressure jump in an idealized case, and, second, flow in our case is inherently unsteady and it is governed by the motion of the flexible surface as a function of time. Therefore, an 'unsteady actuator slab' may be a more appropriate model for our flow. It is worth developing a simple model for the unsteady actuator disc-type action for the kind of flow presented here. We showed that it is the deformation of the flexible surface which causes the unsteady actuator disc-type action and accelerates the near-wake flow in the jet direction. The deformations during the active period are such that they orient the favourable pressure gradient largely in the streamwise direction. In contrast, in the case of a rigid flap/rigid foil, the pressure gradients are expected to be nearly in the transverse direction. The actuator disc-type analysis presented here may be applied to flapping wings both for hovering birds and insects and in forward flight. Velocity fields for such an analysis may be available from experiments (e.g. [21,41,47]) or numerical simulations (e.g. [23,48,49]). Such an analysis might also find applications in the design of artificial hovering devices.

Data accessibility. The additional data can be found in the electronic supplementary material.

Authors' contributions. S.Y.S. fabricated the experimental set-up, conducted the experiments and processed the data. S.Y.S. and J.H.A. analysed the data, interpreted the results and wrote the paper. Both authors gave final approval for publication.

Competing interests. We have no competing interests.

Funding. This work was supported by Naval Research Board grant no. NRBO0013 and AFOSR grant no. AOAD011.

Acknowledgements. We are indebted to Prof. Roddam Narasimha for the critical comments, and Prof. Garry L. Brown, Prof. T. J. Pedley and Dr. Sourabh S. Diwan for the fruitful suggestions. We are grateful to Dr Murali R. Cholemari for the help on PIV measurements. We acknowledge the useful discussions with Prof. R. N. Govardhan and Jim Reeves. We thank the anonymous referees for their valuable inputs.

References

1. Daniel TL, Combes SA. 2002 Flexible wings and fins: bending by inertial or fluid-dynamic forces? *Integr. Comp. Biol.* **42**, 1044. (doi:10.1093/icb/42.5.1044)
2. Wootton RJ. 1999 Invertebrate paraxial locomotory appendages: design, deformation and control. *J. Exp. Biol.* **202**, 3333.
3. Young J, Walker SM, Bomphrey RJ, Taylor GK, Thomas ALR. 2009 Details of insect wing design and deformation enhance aerodynamic function and flight efficiency. *Science* **325**, 1549–1552. (doi:10.1126/science.1175928)
4. Thiria B, Godoy-Diana R. 2010 How wing compliance drives the efficiency of self-propelled flapping flyers. *Phys. Rev. E* **82**, 015303(R). (doi:10.1103/PhysRevE.82.015303)
5. Zhao L, Deng X, Sane SP. 2011 Modulation of leading edge vorticity and aerodynamic forces in flexible flapping wings. *Bioinspir. Biomim.* **6**, 036007. (doi:10.1088/1748-3182/6/3/036007)
6. Harbig R, Sheridan J, Thompson M. 2013 Relationship between aerodynamic forces, flow structures and wing camber for rotating insect wing planforms. *J. Fluid Mech.* **730**, 52–75. (doi:10.1017/jfm.2013.335)
7. Kang C-K, Shyy W. 2014 Analytical model for instantaneous lift and shape deformation of an insect-scale flapping wing in hover. *J. R. Soc. Interface* **11**, 20140933. (doi:10.1098/rsif.2014.0933)
8. Moore MNJ. 2014 Analytical results on the role of flexibility in flapping propulsion. *J. Fluid Mech.* **757**, 599–612. (doi:10.1017/jfm.2014.533)
9. Moore MNJ. 2015 Torsional spring is the optimal flexibility arrangement for thrust production of a flapping wing. *Phys. Fluids* **27**, 091701. (doi:10.1063/1.4930235)
10. Pineirua M, Thiria B, Godoy-Diana R. 2017 Modelling of an actuated elastic swimmer. *J. Fluid Mech.* **829**, 731–750. (doi:10.1017/jfm.2017.570)
11. Tam D. 2015 Flexibility increases lift for passive fluttering wings. *J. Fluid Mech.* **765**, R2. (doi:10.1017/jfm.2015.1)
12. Dewey P, Boschitsch B, Moored K, Stone H, Smits A. 2013 Scaling laws for the thrust production of flexible pitching panels. *J. Fluid Mech.* **732**, 29–46. (doi:10.1017/jfm.2013.384)
13. Gazzola M, Argentina M, Mahadevan L. 2014 Scaling macroscopic aquatic locomotion. *Nat. Phys.* **10**, 758–761. (doi:10.1038/nphys3078)
14. Lucas KN, Johnson N, Beaulieu WT, Cathcart E, Tirrell G, Colin SP, Gemmell BJ, Dabiri JO, Costello JH. 2014 Bending rules for animal propulsion. *Nat. Commun.* **5**, 3293. (doi:10.1038/ncomms4293)
15. Shelton RM, Thornycroft PJM, Lauder GV. 2014 Undulatory locomotion of flexible foils as biomimetic models for understanding fish propulsion. *J. Exp. Biol.* **217**, 2110–2120. (doi:10.1242/jeb.098046)
16. Shyy W, Berg M, Ljungqvist D. 1999 Flapping and flexible wings for biological and micro air vehicles. *Prog. Aerosp. Sci.* **35**, 455–505. (doi:10.1016/S0376-0421(98)00016-5)
17. Triantafyllou MS, Techet AH, Hover FS. 2004 Review of experimental work in biomimetic foils. *IEEE J. Oceanic Eng.* **29**, 585–594. (doi:10.1109/JOE.2004.833216)
18. Freymuth P. 1990 Thrust generation by an airfoil in hover modes. *Exp. Fluids* **9**, 17–24. (doi:10.1007/BF00575331)
19. Wang ZJ, Birch JM, Dickinson MH. 2004 Unsteady forces and flows in low Reynolds number hovering flight: two-dimensional computations vs. robotic wing experiments. *J. Exp. Biol.* **207**, 449–460. (doi:10.1242/jeb.00739)
20. Shinde SY, Arakeri JH. 2013 Jet meandering by a foil pitching in quiescent fluid. *Phys. Fluids* **25**, 041701. (doi:10.1063/1.4800321)
21. Cheng B, Roll J, Liu Y, Troolin DR, Deng X. 2014 Three-dimensional vortex wake structure of flapping wings in hovering flight. *J. R. Soc. Interface* **11**, 20130984. (doi:10.1098/rsif.2013.0984)
22. Heathcote S, Gursul I. 2007 Jet switching phenomenon for a periodically plunging airfoil. *Phys. Fluids* **19**, 027104. (doi:10.1063/1.2565347)

23. Vanella M, Fitzgerald T, Preidikman S, Balaras E, Balachandran B. 2009 Influence of flexibility on the aerodynamic performance of a hovering wing. *J. Exp. Biol.* **212**, 95–105. (doi:10.1242/jeb.016428)
24. Eldredge JD, Toomey J, Medina A. 2010 On the roles of chord-wise flexibility in a flapping wing with hovering kinematics. *J. Fluid Mech.* **659**, 94–115. (doi:10.1017/S0022112010002363)
25. Ristroph L, Childress S. 2014 Stable hovering of a jellyfish-like flying machine. *J. R. Soc. Interface* **11**, 20130992. (doi:10.1098/rsif.2013.0992)
26. David MJ, Govardhan RN, Arakeri JH. 2018 Thrust generation from pitching foils with flexible trailing edge flaps. *J. Fluid Mech.* **828**, 70–103. (doi:10.1017/jfm.2017.491)
27. Park H, Park Y-J, Lee B, Cho K-J, Choi H. 2016 Vortical structures around a flexible oscillating panel for maximum thrust in a quiescent fluid. *J. Fluids Struct.* **67**, 241–260. (doi:10.1016/j.jfluidstructs.2016.10.004)
28. Marais C, Thiria B, Wesfreid J, Godoy-Diana R. 2012 Stabilizing effect of flexibility in the wake of a flapping foil. *J. Fluid Mech.* **710**, 659–669. (doi:10.1017/jfm.2012.390)
29. Shinde SY, Arakeri JH. 2014 Flexibility in flapping foil suppresses meandering of induced jet in absence of free stream. *J. Fluid Mech.* **757**, 231–250. (doi:10.1017/jfm.2014.480)
30. Leishman JG. 2000 *Principles of helicopter aerodynamics*. Cambridge, UK: Cambridge University Press.
31. Weis-Fogh T. 1973 Quick estimates of flight fitness in hovering animals, including novel mechanisms for lift production. *J. Exp. Biol.* **59**, 169–230.
32. Lighthill MJ. 1979 A simple fluid-flow model of ground effect on hovering. *J. Fluid Mech.* **93**, 781–797. (doi:10.1017/S0022112079002032)
33. Rayner JMV. 1979 A vortex theory of animal flight. Part 1. The vortex wake of a hovering animal. *J. Fluid Mech.* **91**, 697–730. (doi:10.1017/S0022112079000410)
34. Ellington CP. 1984 The aerodynamics of hovering insect flight. V. A vortex theory. *Phil. Trans. R. Soc. Lond. B* **305**, 115–144. (doi:10.1098/rstb.1984.0053)
35. Kang C, Aono H, Cesnik C, Shyy W. 2011 Effects of flexibility on the aerodynamic performance of flapping wings. *J. Fluid Mech.* **689**, 32–74. (doi:10.1017/jfm.2011.428)
36. Dai H, Luo H, Paulo JSA, Ferreira S, Doyle JF. 2012 Thrust performance of a flexible low-aspect-ratio pitching plate. *Phys. Fluids* **24**, 101903. (doi:10.1063/1.4764047)
37. Hua R, Zhu L, Lu X. 2013 Locomotion of a flapping flexible plate. *Phys. Fluids* **25**, 121901. (doi:10.1063/1.4832857)
38. Shinde SY. 2012 Creation of an orderly jet and thrust generation in quiescent fluid from an oscillating two-dimensional flexible foil. PhD thesis, Indian Institute of Science, Bangalore, India.
39. Taylor GI. 1953 Formation of a vortex ring by giving an impulse to a circular disk and then dissolving it away. *J. Appl. Phys.* **24**, 104. (doi:10.1063/1.1721114)
40. Lighthill MJ. 1973 On the Weis-Fogh mechanism of lift generation. *J. Fluid Mech.* **60**, 1–7. (doi:10.1017/S0022112073000017)
41. Wolf M, Ortega-Jimenez VM, Dudley R. 2013 Structure of the vortex wake in hovering Anna's hummingbirds (*Calypte anna*). *Proc. R. Soc. B* **280**, 20132391. (doi:10.1098/rspb.2013.2391)
42. Ellington CP. 1984 The aerodynamics of hovering insect flight. I. The quasi-steady analysis. *Phil. Trans. R. Soc. Lond. B* **305**, 1–15. (doi:10.1098/rstb.1984.0049)
43. Ellington CP. 1984 The aerodynamics of hovering insect flight. IV. Aeorodynamic mechanisms. *Phil. Trans. R. Soc. Lond. B* **305**, 41–78. (doi:10.1098/rstb.1984.0051)
44. Bohl DG, Koochesfahani MM. 2009 MTV measurements of the vortical field in the wake of an airfoil oscillating at high reduced frequency. *J. Fluid Mech.* **620**, 63–88. (doi:10.1017/S0022112008004734)
45. Glauert H. 1935 Airplane propellers. In *Aerodynamic theory IV* (ed. WF Durand). Berlin, Germany: Julius Springer.
46. Zhao L, Huang Q, Deng X, Sane SP. 2010 Aerodynamic effects of flexibility in flapping wings. *J. R. Soc. Interface* **7**, 485–497 (doi:10.1098/rsif.2009.0200)
47. Hawkes EW, Lentink D. 2016 Fruit fly scale robots can hover longer with flapping wings than with spinning wings. *J. R. Soc. Interface* **13**, 20160730. (doi:10.1098/rsif.2016.0730)
48. Nakata T, Liu H. 2012 Aerodynamic performance of a hovering hawkmoth with flexible wings: a computational approach. *Proc. R. Soc. B* **279**, 722–731. (doi:10.1098/rspb.2011.1023)
49. Zheng L, Hedrick T, Mittal R. 2013 A comparative study of the hovering efficiency of flapping and revolving wings. *Bioinspir. Biomim.* **8**, 036001. (doi:10.1088/1748-3182/8/3/036001)